

Electromagnetic Induction Imaging with Atomic Magnetometers : Report

Master Project at University College London

Master Student Boris Baudel

Department of Mechatronics, Ecole normale supérieure Rennes, France

Prof. Ferruccio Renzoni

Department of Physics and Astronomy, University College London, UK

Dr. Yao Han

Department of Physics and Astronomy, University College London, UK

Msc Junxing, Msci Student at UCL

Msc Liu Yufei, Zhejiang University of Technology, China

Msc Jiang Chuzheng, Imperial College London, UK

Msc Zhao Longjie, Msci Student at UCL



Figure 1: Laser cooling group



Contents

1. Introduction	3
2. Functioning of the current system : State of art	3
2.1 Electromagnetic Induction Imaging	4
2.2 The Zeeman effect	4
2.2.1 Energy Level Displacement	4
2.2.2 Operation and Frequency Determination	5
2.3 Skin Effect	5
3. Optical Set up	6
3.1 Introduction for Optical Set up	6
4. Quantum optics approach	8
4.1 Liouville Equation in our system	8
4.1.1 Hamiltonian Commutator $\frac{1}{i\hbar}[H, \rho]$	8
4.1.2 Optical Pumping Term $\Gamma_{\text{op}}[\phi(1 + 2s \cdot S) - \rho]$ and Spin-Exchange Collision Term $\Gamma_{\text{se}}[\phi(1 + 4hS_i \cdot S) - \rho]$	8
4.1.3 Diffusion Term $D\nabla^2\rho$ and Hamiltonian	8
5. Data processing	8
5.1 The Matlab processing code	8
5.1.1 Lorentzian Derivative	9
5.1.2 The R function	10
5.2 Image processing	10
6. Results	10
6.0.1 Two photon configuration : 300kHz	10
6.0.2 Optimization	11
6.0.3 Image results	12
7. Conclusion	12
8. Bibliography	13
9. Appendix	14
9.1 Magnetic resonance Measurement	14
9.2 Nuclear atomic resonance in our conditions	15
9.2.1 Bloch Equations Description	15
9.2.2 Steady-State Solutions to the Bloch Equations	16
9.2.3 Predicted Resonance Line Shapes	16
9.3 Helmholtz coil effect on the Zeeman Effect	17

1. Introduction

Electromagnetic induction imaging (EMI) non-invasively maps materials' electromagnetic properties using a radio-frequency magnetic field to probe samples and record the induced eddy current response. The performance of an EMI system hinges on the magnetic field sensor's sensitivity, frequency range, and sensing volume. Atomic magnetometers (AMs), particularly radio-frequency atomic magnetometers (RF-AMs), are ultra-sensitive to oscillating magnetic fields, making them ideal for EMI applications. This work focuses on developing EMI systems with RF-AMs, achieving high-resolution imaging across various materials.[1]

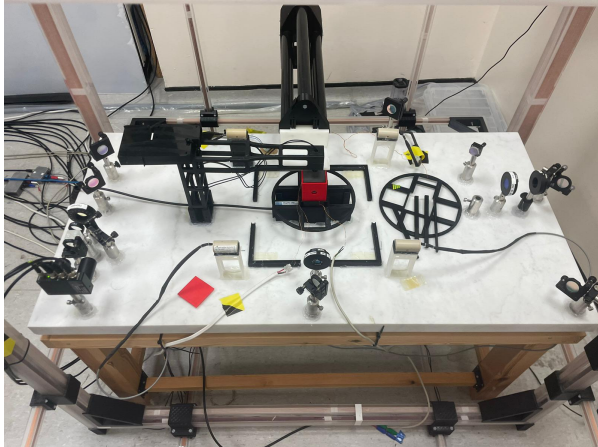


Figure 2: The real system in induction configuration

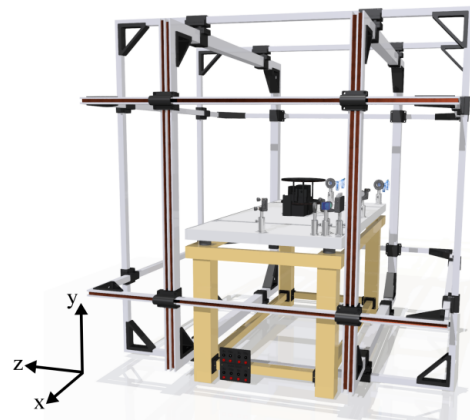


Figure 3: The system with the Helmholtz and anti Helmholz coils

A single-channel rubidium RF-AM was developed, operating near room temperature with a sensitivity of 55 fT/Hz and a linewidth of 36 Hz, effective across the kHz-MHz band. The small sensor volume enhances spatial resolution. High-resolution EMI was demonstrated on materials with conductivities ranging from 6.10^7 Sm^{-1} to 500 Sm^{-1} , with sample volumes of a few cm^3 and an imaging resolution of around 1 mm. Techniques like multi-frequency image analysis and machine learning-based reconstruction were used to enhance imaging. The feasibility of biomedical applications, such as imaging heart conductivity, was also verified through simulations [1].

2. Functioning of the current system : State of art

The general principle behind Electromagnetic Induction (EMI) is depicted in the Argand diagram shown in Figure 5. An alternating current (AC) magnetic field, referred to as the primary field (B_1), is applied to induce eddy currents within a conductive sample. Eddy currents are circular loops of current that arise in response to a changing magnetic field, as dictated by Faraday's law of induction. The density and flow of these currents depend on the dielectric properties and the geometric configuration of the sample. This flow of electrons, in turn, generates an additional oscillating magnetic field component, known as the secondary field (B_2), which opposes the primary field as per Lenz's law. The characteristics of the eddy current flow, which are determined by the electromagnetic properties of the sample, influence the properties of B_2 . Consequently, B_2 can be related to the sample's electrical conductivity (σ), relative permittivity (ϵ_r), and relative permeability (μ_r) [1].

2.1 Electromagnetic Induction Imaging

The interaction between the primary and secondary fields results in a total field (B_{tot}). This combined effect is detected using a magnetic field sensor, allowing the properties of B_2 to be inferred and the electromagnetic properties of the sample to be extracted.

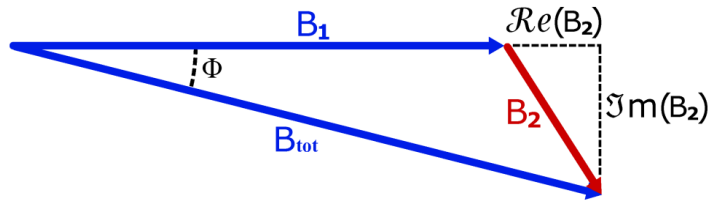


Figure 4: Argand diagram illustrating the principle of EMI

One of the main challenges in EMI systems lies in detecting and correctly attributing the contributions of the secondary field. Generally, the magnitude of B_2 is significantly smaller than that of B_1 . Thus, a highly sensitive and stable magnetometer is required to accurately detect and measure these subtle variations.

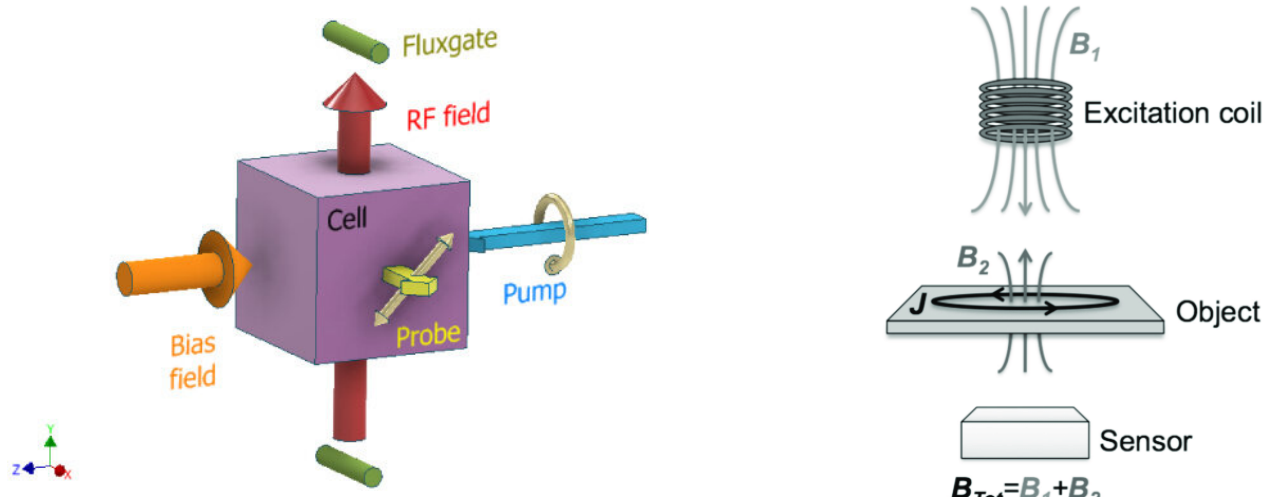


Figure 5: Probe, pump, Bias field, RF field in the atomic magnetometer

Figure 6: Primary and secondary fields

2.2 The Zeeman effect

The Zeeman effect describes how a static magnetic field perturbs the hyperfine structure of atomic energy levels, forming the operational basis of all atomic magnetometers (AMs). In the absence of a magnetic field, magnetic sub-levels are degenerate. When a magnetic field is applied, these sub-levels split, representing different projections of the atomic angular momentum onto the quantization axis defined by the magnetic field, \mathbf{B} . Specifically, for the Radio Frequency Atomic Magnetometer (RF-AM), a controlled DC field B_z is applied along the z-direction, commonly referred to as the bias field $B_{\text{bias}} = B_{\text{bias}}^z$.

2.2.1 Energy Level Displacement

In the presence of a weak magnetic field, the energy levels are evenly displaced. For a state $|F, m_F\rangle$, the change in energy is expressed as:

$$\Delta E_{|F, m_F\rangle} = g_F \mu_B m_F B, \quad (1)$$

where μ_B is the Bohr magneton and g_F is the hyperfine Landé g-factor. The hyperfine Landé g-factor can be well approximated by:

$$g_F \approx \frac{F(F+1) - I(I+1) + J(J+1)}{2F(F+1)} g_J, \quad (2)$$

with g_J representing the total angular momentum Landé g-factor.

2.2.2 Operation and Frequency Determination

The RF-AM experiments discussed in subsequent chapters typically operate in magnetic fields below 5 Gauss, a regime where the weak-field approximation of Equation 1 remains valid. The Zeeman effect determines the operating frequency of an RF-AM as follows:

$$\nu_L = \frac{\Delta E_{|F,m_F+1\rangle} - \Delta E_{|F,m_F\rangle}}{\hbar} = 2\pi\gamma B_{\text{bias}}, \quad (3)$$

where γ is the gyromagnetic ratio.

An RF field oscillating at ν_L coherently drives the Zeeman (or RF) transitions within the same hyperfine level ($\Delta F = 0$), transferring atoms between different magnetic sub-levels. This process induces atomic precession, a fundamental mechanism in RF-AM operation.

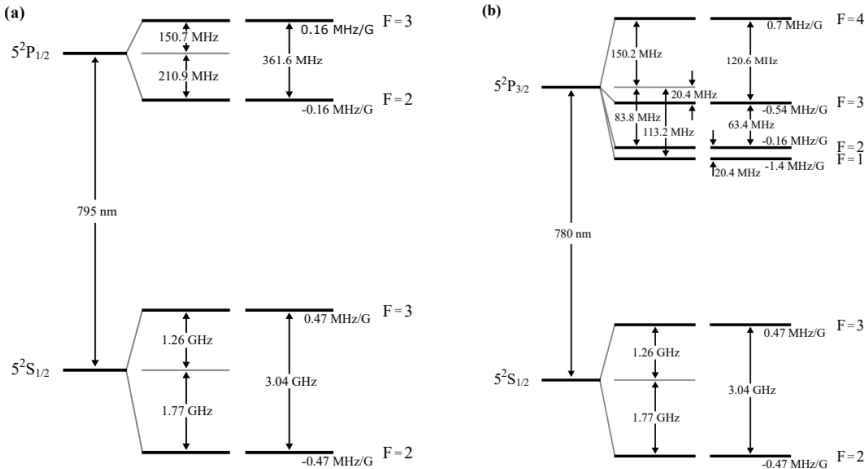


Figure 7: Helmholtz coil effect on the Zeeman Effect

2.3 Skin Effect

The skin effect is a phenomenon where the current density is predominantly concentrated near the surface due to eddy current flow and decreases exponentially with depth. Firstly, the flow of eddy currents generates a secondary field response that opposes the primary field, leading to a reduced propagation of the primary field into deeper layers, and hence, a reduction in current density at those depths. Alternatively, the skin effect can be viewed as the conversion of energy from the primary field into eddy current flow, causing a decrease in field energy as it propagates into the material and consequently reducing eddy current generation. The current density at a depth y (denoted J_y) is described by:

$$J_y = J_0 e^{-y/\delta(\omega)} \quad (1)$$

where J_0 is the surface current density, and $\delta(\omega)$, the skin depth, is the depth at which the current density reduces to J_0/e . This relationship is scaled by $\delta(\omega)$ and current density by J_0 . In the idealized model, the phase lag (Φ) between the primary field at the surface and the eddy current density at depth y is expressed in radians as:

$$\Phi = \frac{y}{\delta(\omega)} \quad (2)$$

The formula for the skin depth is given by:

$$\delta(\omega) = \sqrt{\frac{1}{\omega\mu\epsilon \left(\frac{1}{2} \left(\sqrt{1 + \left(\frac{\sigma}{\omega\epsilon} \right)^2} - 1 \right) \right)}} \quad (3)$$

where $\mu = \mu_r \mu_0$, and $\epsilon = \epsilon_r \epsilon_0$ (with ϵ_0 and μ_0 being the permittivity and permeability of free space, respectively) [1][2].

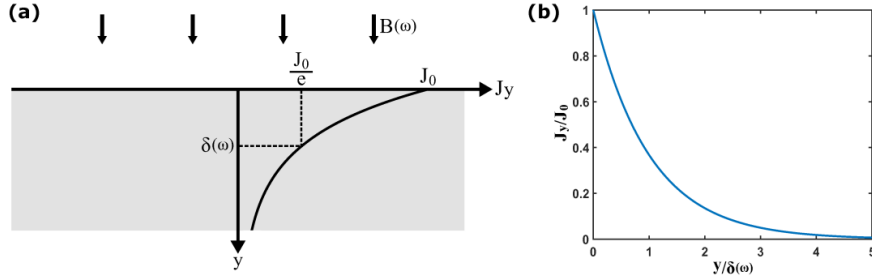


Figure 8: Skin effect on the sample

3. Optical Set up

3.1 Introduction for Optical Set up

A schematic sketch of the unshielded RF-AM setup is shown in Figure 4.1. The arrangement follows that first described by Savukov et al. (2005) [8]. At the heart of the sensor, an alkali vapor cell containing Rb is used. The atomic vapor is spin-polarized by optical pumping. This is accomplished by the application of a circularly polarized pump beam and a parallel DC magnetic field (the bias field – B_{BIAS}). The direction of the pump beam is defined as the z-direction. The σ_+ polarization of the pump beam is prepared immediately before the cell using a quarter-wave plate ($\lambda/4$).

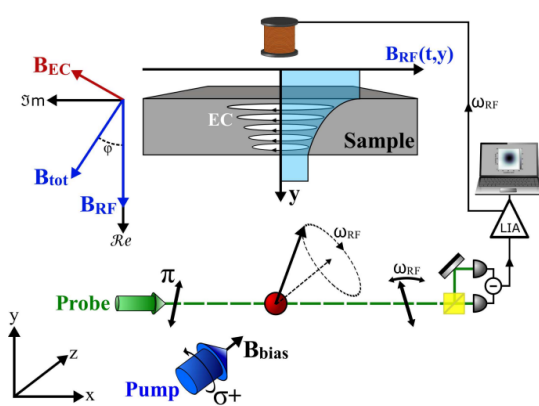


Figure 9: Probe, pump, Bias field, RF field in the atomic magnetometer

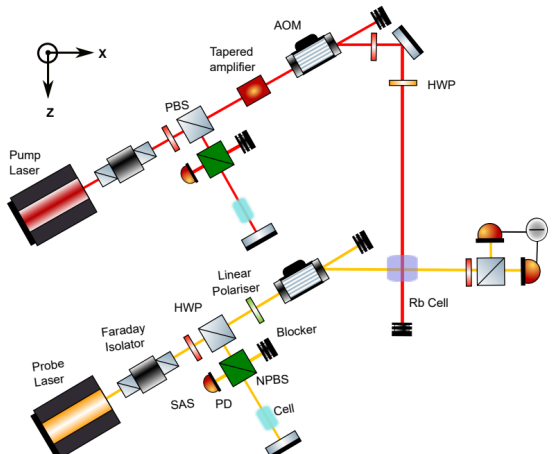


Figure 10: Probe, pump for the laser lightpath

The bias field is controlled by a series of Helmholtz coils. The magnitude of this field sets the operating frequency of the RF-AM – a consequence of the Zeeman effect. In this way, the operating frequency can be tuned in light of the desired application. The magnetometer is calibrated with a known AC magnetic field (B_{RF}) in the y-direction. This field excites spin coherences between nearest-neighbour ground state Zeeman sub-levels, producing a transverse atomic polarization rotation. The atomic precession is read out by the rotation of the plane of polarization of a linearly polarized probe beam. This crosses perpendicular to the pump beam at the center of the cell. The overlapping

region defines the sensing volume. The perpendicular arrangement allows fine control over the size of the sensing region, balancing the signal (larger with a larger sensing volume) and the spatial resolution of the measurements (greater with a smaller sensor). The probe beam is usually blue-detuned from the reference transition to minimize the disturbance of the atomic polarization. The linear polarization of the probe beam is set by a half-wave plate ($\lambda/2$) before the beam propagates through the cell in the x-direction.

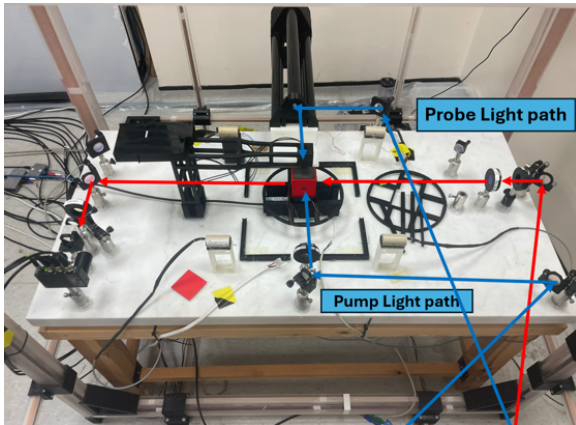


Figure 11: Probe, pump for the laser lightpath singlepass for the probe

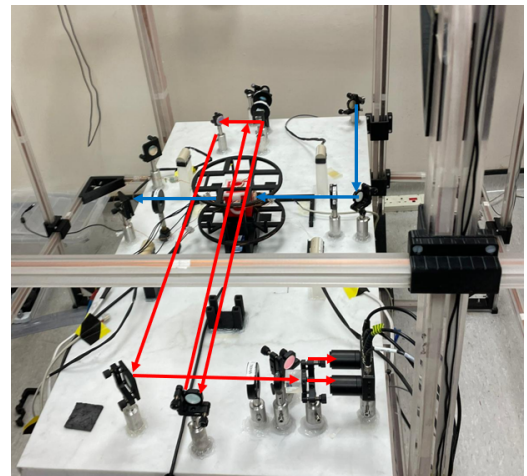


Figure 12: Probe, pump for the laser lightpath doublepass for the probe

The polarimeter, consisting of a polarizing beam splitter and a balanced photodiode (Thorlabs PDB210A), detects the probe beam's polarization rotation. The output of the photodiode is interrogated by a lock-in amplifier (LIA, Ametek 7280 DSP) and a spectrum analyzer (SA, Anritsu MS2718B). The LIA simultaneously extracts four streams of data: the in-phase (absorptive, X) and out-of-phase (dispersive, Y) components of the polarimeter along with the radius $R \equiv \sqrt{X^2 + Y^2}$ and phase $\Phi \equiv \arctan(Y/X)$. The desired outputs of the LIA (X, Y, R, and Φ) and the spectrum traces recorded by the SA are acquired on a laptop.

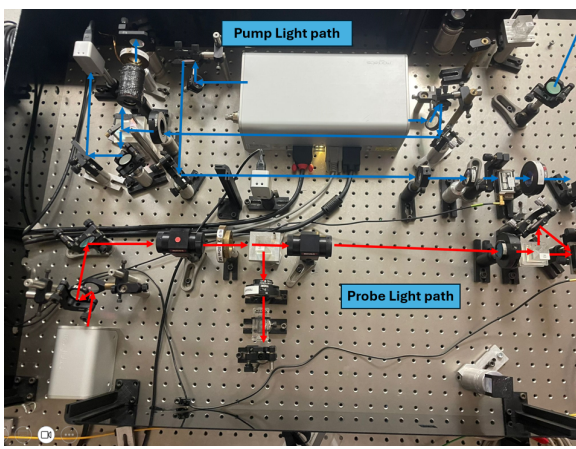


Figure 13: Pump and probe lightpath

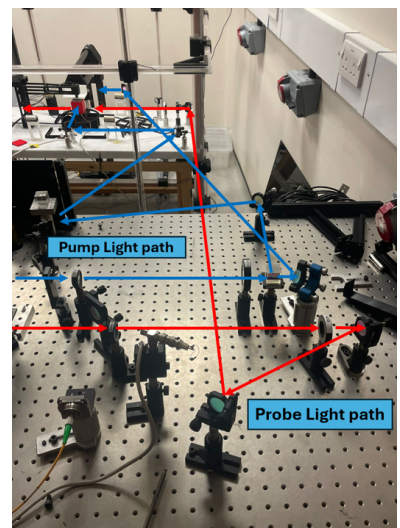


Figure 14: Pump and probe lightpath

4. Quantum optics approach

4.1 Liouville Equation in our system

To fully characterize the atomic system, a density matrix approach is required. This is comprehensively described in Appelt et al. (1998) [9], where the evolution of the density matrix for the RF-AM system is given by:

$$\frac{d\rho}{dt} = \frac{1}{i\hbar}[H, \rho] + \Gamma_{\text{op}}[\phi(1 + 2s \cdot S) - \rho] + \Gamma_{\text{se}}[\phi(1 + 4hS_i \cdot S) - \rho] + D\nabla^2\rho, \quad (3.52)$$

with only the terms that account for the significant processes in the system included.

4.1.1 Hamiltonian Commutator $\frac{1}{i\hbar}[H, \rho]$

This term represents the primary quantum mechanical evolution of the system under its Hamiltonian H . The commutator $[H, \rho]$ dictates how the state of the system is influenced by its total energy operator. The prefactor $\frac{1}{i\hbar}$ ensures that the evolution is unitary, which is a fundamental requirement in quantum mechanics.

4.1.2 Optical Pumping Term $\Gamma_{\text{op}}[\phi(1 + 2s \cdot S) - \rho]$ and Spin-Exchange Collision Term $\Gamma_{\text{se}}[\phi(1 + 4hS_i \cdot S) - \rho]$

This describes the impact of optical pumping, a technique used to manipulate the population of quantum states via light. Γ_{op} is the rate at which this process occurs. The target state influenced by the optical pumping is represented by ϕ , and $1 + 2s \cdot S$ modifies this target based on the interaction between the spin vectors s and S , indicating the alignment towards a specific polarization. Γ_{se} represents the rate of spin-exchange collisions, a phenomenon where the spins of particles are exchanged during interactions. This term modifies the density matrix towards an equilibrium state defined by ϕ , altered by $1 + 4hS_i \cdot S$, reflecting more intense or different spin interactions compared to optical pumping.

4.1.3 Diffusion Term $D\nabla^2\rho$ and Hamiltonian

The diffusion coefficient D and the Laplacian $\nabla^2\rho$ together describe the spatial diffusion of the state properties within the system. This term is responsible for the spreading and evening out of quantum state properties across the physical system, relevant in non-uniform or spatially extended quantum systems. The first term is the Liouville equation describing the free evolution under the Hamiltonian, H , defined as:

$$H = H_g + H_{\text{rf}}, \quad (3.53)$$

where H_g is the ground state Hamiltonian. It includes the hyperfine structure and the magnetic-dipole coupling between the bias field and both the electron and nuclear spins. H_{rf} is the Hamiltonian for the interaction between the electron spin and RF field:

$$H_{\text{rf}} = 2g_s\mu_B S_x B_1 \cos(\omega t), \quad (3.54)$$

where g_s is the electron g-factor.

5. Data processing

5.1 The Matlab processing code

The given algorithm outlines a method for fitting Lorentzian curves to data points for interpreting magnetic resonance signals. The algorithm processes multidimensional input data and applies Lorentzian and derivative models to each pixel performing least-squares optimization.. This allows for a detailed

analysis of the lineshapes of the transverse spin components, represented as \tilde{S}_x and \tilde{S}_y , in a magnetic field. The Lorentzian lineshape for the \tilde{S}_x component is described by the formula:

$$\tilde{S}_x(\omega_{RF}) = S_0 B_{RF} \gamma \frac{\Gamma}{4[(\omega_{RF} - \Omega_L)^2 + \Gamma^2/4]},$$

which is centered on the Larmor frequency Ω_L with a linewidth Γ indicating the system's sensitivity. This response is crucial for determining the properties of the magnetic field by analyzing the detected frequency shifts [1][2]. Similarly, the dispersive component, \tilde{S}_y , which provides complementary information about the magnetic field dynamics, is given by:

$$\tilde{S}_y(\omega_{RF}) = S_0 B_{RF} \gamma \frac{(\Omega_L - \omega_{RF})}{2[(\omega_{RF} - \Omega_L)^2 + \Gamma^2/4]},$$

The script employs the `curve_fit` function from `scipy.optimize` to fit the Lorentzian model and its derivative to subsets of spectral data. Initial guesses ($p0$) and bounds are set to guide the fitting process, which is crucial for achieving accurate fits in nonlinear regression. The Lorentzian function is widely used in spectroscopy to model resonance phenomena. The function is defined as:

$$f(x) = \frac{A\gamma^2}{\gamma^2 + (x - x_0)^2} + C \quad (4)$$

5.1.1 Lorentzian Derivative

The derivative of the Lorentzian function is used to analyze the changes in the spectral line shape, which can be particularly useful for detecting inflection points or subtle shifts in signal behavior:

$$f'(x) = \frac{A\gamma(x - x_0)}{\gamma^2 + (x - x_0)^2} + C \quad (5)$$

The script calculates the magnitude (r) and phase (ϕ) from the fitted parameters as follows:

$$r = \sqrt{x_{\text{mid}}^2 + y_{\text{mid}}^2} \quad (6)$$

$$\phi = \arctan \left(\frac{y_{\text{mid}}}{x_{\text{mid}}} \right) \quad (7)$$

where x_{mid} and y_{mid} are the coordinates derived from the fits at specific frequencies, representing physical properties such as the amplitude and phase shift of a resonance peak. The script processes multiple sets of data (1681 sets, suggesting a 41x41 grid), fitting models to the data, extracting parameters, and computing derived quantities in each iteration.

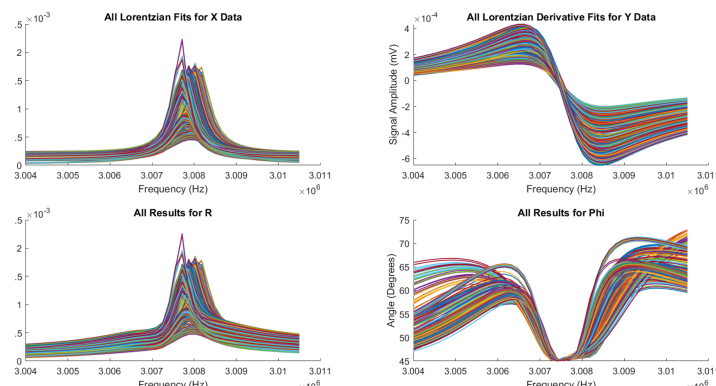


Figure 15: Lorentzian and Lorentzian derivative for the feating function

5.1.2 The R function

The script saves data including resonance frequencies, magnitudes, and phases to a file for further analysis or visualization.

The R-squared function is defined as:

$$R^2 = 1 - \frac{\text{sum of squares of residuals}}{\text{total sum of squares}} = 1 - \frac{\sum(y_{\text{pred}} - y_{\text{true}})^2}{\sum(y_{\text{true}} - \bar{y}_{\text{true}})^2} \quad (8)$$

This measure quantifies how well the observed data are replicated by the model, providing an indication of the fit quality.

5.2 Image processing

The Gaussian filter is an image processing technique that smooths or blurs an image by applying a convolution with a Gaussian function. This operation reduces noise and fine details while preserving the overall structures of the image. The two-dimensional Gaussian function is defined by a bell-shaped curve centered at the origin, with its width determined by the standard deviation, σ . A larger σ results in more intense smoothing. Convolution is a mathematical operation that combines two functions to produce a third function. In image processing, it is used to apply filters to images. For an image I and a filter K of size $m \times n$, the convolution is calculated by summing the products of the image values and the shifted filter values based on the coordinates. Cubic interpolation uses cubic polynomials to estimate values between known data points. We can also develop an algorithm that can calculate the distance between two holes as shown in the figure below. We can test the algorithm on some images and datasets [1][2].

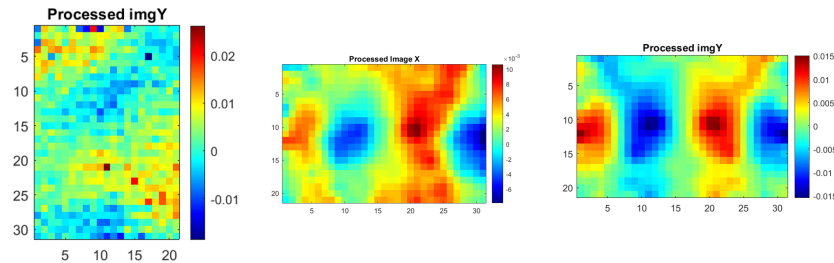


Figure 16: Raw data, Gaussian filtering with $\sigma = 1$, and image with gradient remover function

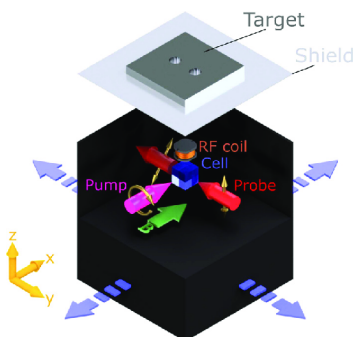


Figure 17: Portable magnetometer [4]

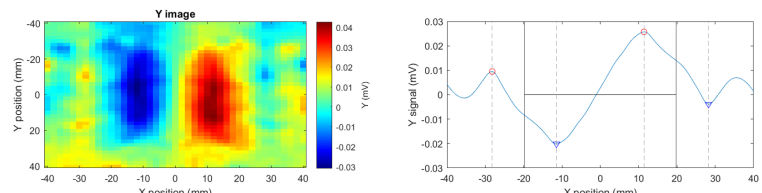


Figure 18: Two holes distance results for the second data set : 36,5mm

6. Results

6.0.1 Two photon configuration : 300kHz

In the two-photon configuration, two RF photons with distinct polarizations are employed. This method exploits the principle that π -polarized RF photons induce π transitions, whereas σ -polarized

photons facilitate σ transitions. The scheme incorporates an additional RF field, B_c , which propagates along B_{Bias} and enables a two-photon transition at a designated frequency. The interaction of the σ -polarized B_{RF} photon with the π -polarized B_c photon satisfies the selection rule $\Delta m = \pm 1$, thereby coupling adjacent magnetic sublevels. By tuning ω_c , the RF-AM resonance can be effectively shifted relative to ω_{RF} , without modifying B_{Bias} . The Rabi frequency for this two-photon transition, as detailed by Geng et al, retains the linearity in Ω_{RF} characteristic of the standard RF-AM setup, but incorporates an additional factor [7].

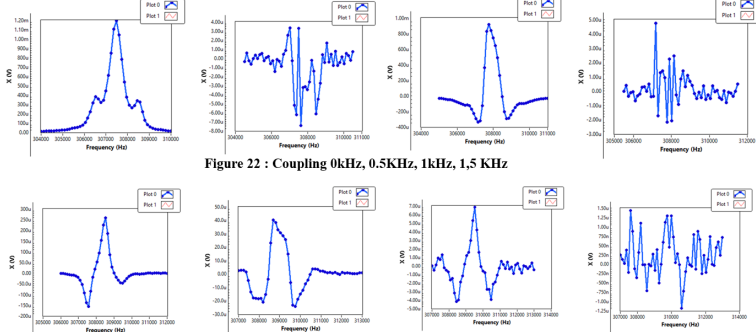


Figure 22 : Coupling 0kHz, 0.5kHz, 1kHz, 1.5kHz

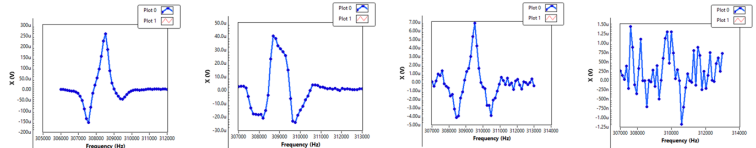


Figure 23 : Coupling 2 kHz , 3 kHz , 4 kHz, 5 kHz

Figure 19: Signals results in function of different coupling frequencies [7]

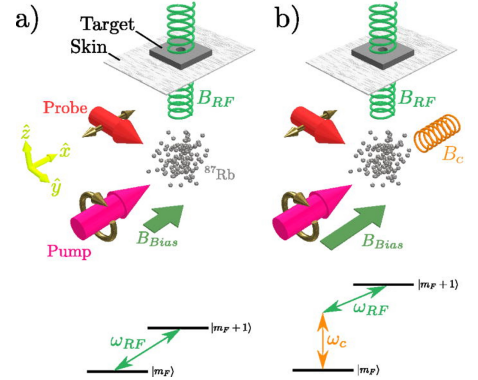


Figure 20: Two photon configuration for an Atomic magnetometer [7]

6.0.2 Optimization

The presented charts depict the relationship between RF sensitivity and various parameters—PR, PU, RF, and temperature—utilizing linear and polynomial regressions. The overarching goal is to minimize RF sensitivity, thereby enhancing device performance. Increasing PR results in a linear reduction in RF sensitivity. Conversely, RF sensitivity escalates with higher RF values. A polynomial relationship with PU suggests there is an optimal value of PU that minimizes RF sensitivity, while lower temperatures are significantly effective in reducing RF sensitivity. Achieving the lowest possible RF sensitivity involves increasing PR to leverage its negative correlation with sensitivity, actively managing temperature to ensure low levels, adjusting PU to the identified optimal point, and limiting high RF values to prevent increases in sensitivity.

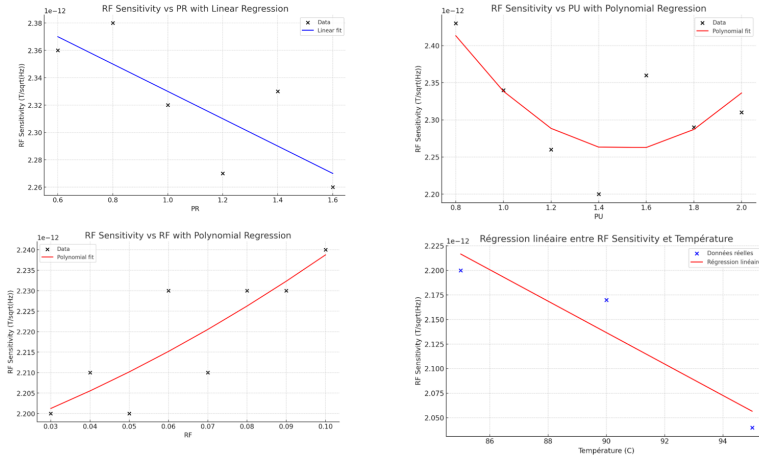


Figure 21: Optimization results

The described experimental conditions involve a 300 MHz Single Path Probe and Single Path Pump, operating in an environment controlled using optical modulation via Acousto-Optic Modulators (AOMs). RF sensitivity setting include a field strength of 2.05×10^{-12} . An additional RF parameter

set at 0.1. The AOM for the pump is adjusted to 1.4 volts, and for the probe, it is set slightly higher at 1.6 volts. These voltages control the modulation of laser beams used in each path, affecting the frequency, intensity, and directionality of the lasers via sound waves generated within the AOM. We are operating at a temperature of 100 degrees Celsius [1] [2].

6.0.3 Image results

Measuring from the center where the disturbance is greatest to the outer edges where the effect dissipates can give a precise measurement of the coin's diameter. The intensity and spread of the eddy currents, as represented in the images, should correlate well with the physical dimensions of the coin. Eddy currents are circular electric currents induced within conductors by a changing magnetic field in the conductor, as described by Lenz's law.

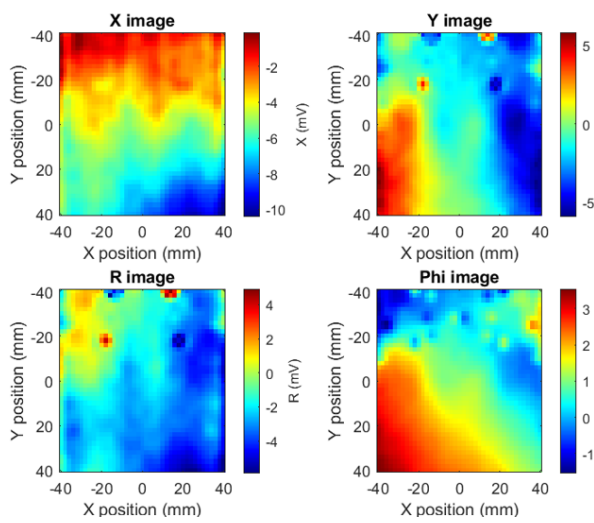


Figure 22: Imaging results for the first data set

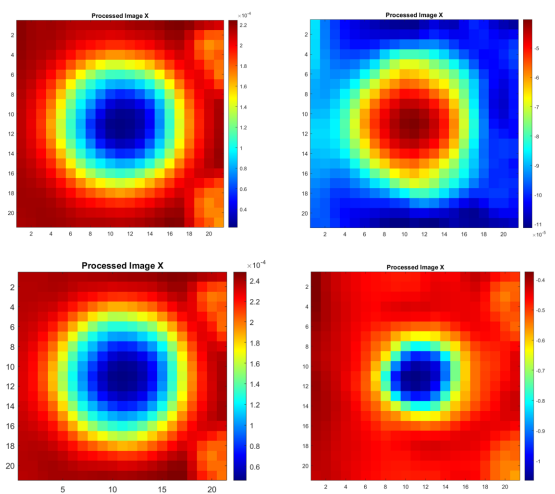


Figure 23: Imaging results for the copper coin with an RF sensitivity of 2.05×10^{-12}

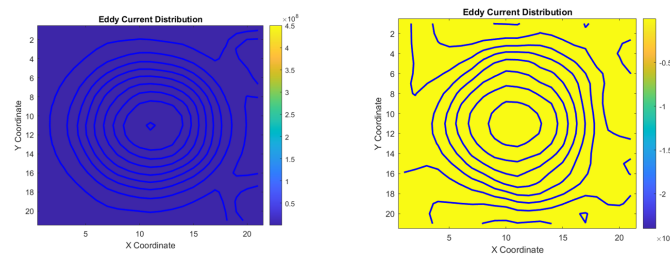


Figure 24: Eddy currents in X and Y signals

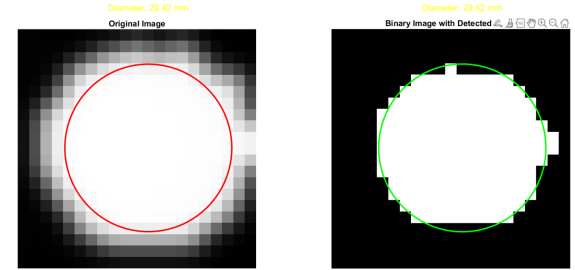


Figure 25: Size estimation of 2.997 cm

7. Conclusion

This study enhances magnetic field detection using atomic magnetometers (AMs) in electromagnetic induction imaging (EMI), focusing on single-channel rubidium RF-AMs. These advancements are promising for biomedical imaging (2 MHz). Additionally, the introduction of a two-photon transition configuration with distinct polarizations refines magnetic resonance imaging, expanding theoretical and practical capabilities. This research explains sensing and material characterization, integrating with emerging quantum sensing technologies. These improvements could significantly impact scientific and medical fields, enhancing our ability to visualize and measure magnetic phenomena.

8. Bibliography

- [1] Deans, C. (2018). *Electromagnetic Induction Imaging with Atomic Magnetometers*. Doctoral dissertation, University College London, Department of Physics and Astronomy.
- [2] Yao, H. (2023). *High-sensitivity unshielded radio-frequency atomic magnetometers*. Doctoral dissertation, University College London, Department of Physics and Astronomy.
- [3] Deans, C., Marmugi, L., Hussain, S., Renzoni, F. (2016). *Electromagnetic induction imaging with a radio-frequency atomic magnetometer*. Applied Physics Letters, 108(10):103503. doi:10.1063/1.4943659.
- [4] Marmugi, L., Gori, L., Hussain, S., Deans, C., Renzoni, F. (2017). *Remote detection of rotating machinery with a portable atomic magnetometer*. Applied Optics, 56(3):743–749. doi:10.1364/AO.56.000743.
- [5] Deans, C., Marmugi, L., Renzoni, F. (2017). *Through-barrier electromagnetic imaging with an atomic magnetometer*. Optics Express, 25(15):17911–17917. doi:10.1364/OE.25.017911.
- [6] Deans, C., Marmugi, L., Renzoni, F. (2018). *Active underwater detection with an array of atomic magnetometers*. Applied Optics, 57(10):2346–2351. doi:10.1364/AO.57.002346.
- [7] Maddox, B., Renzoni, F. (2023). *Two-photon electromagnetic induction imaging with an atomic magnetometer*. Applied Physics Letters, 122(14). doi:10.1063/5.0147291.
- [8] I. M. Savukov, S. J. Seltzer, M. V. Romalis, and K. L. Sauer. *Tunable atomic magnetometer for detection of radio-frequency magnetic fields*. Physical Review Letters, 95(6):063004, 2005. doi:10.1103/PhysRevLett.95.063004.
- [9] S. Appelt, A. B. Baranga, C. J. Erickson, M. V. Romalis, et al. *Theory of spin-exchange optical pumping of ^3He and ^{129}Xe* . Physical Review A, 58(2):1412, 1998. doi:10.1103/PhysRevA.58.1412.

9. Appendix

9.1 Magnetic resonance Measurement

In the RF magnetometer, a collection of atoms optically pumped along a static field B_{Bias} becomes subject to a perpendicularly aligned radio-frequency (RF) magnetic field B_{RF} at a frequency of ω_{RF} . Figure 6 shows the geometry of the RF magnetometer with respect to the atomic source. A circularly polarised pump beam propagates parallel to B_{Bias} in the y -axis, and the sample is probed by a linearly polarised probe beam in the x -axis. When $\omega_{\text{RF}} = \Omega_L = \gamma B_{\text{Bias}}$, the ground state magnetic sublevel populations are coupled by the RF field, allowing transfer between them, which then imprints an oscillating polarisation rotation onto the probe beam at ω_{RF} . Figure 2.3b shows an illustrative depiction of this process in the ground state in the $F = 2$ state of ^{87}Rb . The ensemble of atoms gets pumped towards the stretched $|F = 2, m_F = 2\rangle$ state, creating the population anisotropy in the ground state, for B_{RF} to couple together for population transfer. The RF magnetometer response can be modelled with the Bloch equations as is done in several previous works. The collective spin vector for the atomic ensemble can be written as $S = S_x \hat{x} + S_y \hat{y} + S_z \hat{z}$.

$$\frac{dS}{dt} = \gamma S \times B - \frac{S_x \hat{x} + S_y \hat{y}}{T_2} - \frac{(S_z - S_0) \hat{z}}{T_1}, \quad (9)$$

where γ is the gyromagnetic ratio. The three terms on the right-hand side of equation (9) represent the kinetic evolution of the spins in the field, the transverse spin relaxation with decay time T_2 , and the longitudinal spin relaxation towards the equilibrium state S_0 with decay time T_1 . In the RF magnetometer, the applied magnetic fields become the sum of the static bias field and the perpendicularly applied RF field, such that the magnetic field is

$$B = B_{\text{Bias}} + B_{\text{RF}} = B_{\text{Bias}} \hat{z} + 2B_1 \cos(\omega_{\text{RF}} t) \hat{y}, \quad (10)$$

where $2B_1 = B_{\text{RF}}$. We now move to the rotating frame about \hat{z} at a frequency ω_{RF} and make the rotating wave approximation; tilde notation above the symbols now indicates the quantity in the rotating frame. The effective magnetic field in the rotating frame B_{eff} then becomes

$$B_{\text{eff}} = \left(B_{\text{Bias}} + \frac{\omega_{\text{RF}}}{\gamma} \right) \hat{z} + B_1 \hat{y} = \frac{1}{\gamma} (\Delta\omega \hat{z} + \Omega_1 \hat{y}), \quad (11)$$

where $\Omega_1 = \gamma B_1$ is the Larmor frequency of the field B_1 and $\Delta\omega = \omega_{\text{RF}} - \Omega_L$ is the detuning of the magnetometer from the Larmor frequency of B_{Bias} . The counter-rotating component of the RF field is neglected under the rotating wave approximation. Now the evolution of the total spin vector in the rotating frame \tilde{S} can be expressed as

$$\frac{d\tilde{S}}{dt} = \tilde{S} \times B_{\text{eff}} - \frac{\tilde{S}_x \hat{x} + \tilde{S}_y \hat{y}}{T_2} - \frac{(\tilde{S}_z - S_0) \hat{z}}{T_1}. \quad (12)$$

The rate equations for each component of \tilde{S} can then be summarised by

$$\begin{pmatrix} \frac{d\tilde{S}_x}{dt} \\ \frac{d\tilde{S}_y}{dt} \\ \frac{d\tilde{S}_z}{dt} \end{pmatrix} = \begin{pmatrix} -\frac{1}{T_2} & \Delta\omega & -\Omega_1 \\ -\Delta\omega & -\frac{1}{T_2} & 0 \\ \Omega_1 & 0 & -\frac{1}{T_1} \end{pmatrix} \begin{pmatrix} \tilde{S}_x \\ \tilde{S}_y \\ \tilde{S}_z \end{pmatrix} + \begin{pmatrix} 0 \\ 0 \\ \frac{S_0}{T_1} \end{pmatrix}.$$

Under the condition of steady state where $\frac{d\tilde{S}_x}{dt} = \frac{d\tilde{S}_y}{dt} = \frac{d\tilde{S}_z}{dt} = 0$, the differential equations for each component have the solution

$$\tilde{S}_x = \frac{\gamma B_1 T_2}{1 + \gamma^2 B_1^2 T_1 T_2 + \Delta\omega^2 T_2^2} S_0,$$

$$\tilde{S}_y = \frac{-\gamma \Delta\omega B_1 T_2^2}{1 + \gamma^2 B_1^2 T_1 T_2 + \Delta\omega^2 T_2^2} S_0,$$

$$\tilde{S}_z = \frac{1 + \Delta\omega^2 T_2^2}{1 + \gamma^2 B_1^2 T_1 T_2 + \Delta\omega^2 T_2^2} S_0.$$

Now by making the substitution

$$\Gamma = \frac{2}{T_2} \sqrt{1 + \frac{\gamma^2 B_{\text{RF}}^2 T_1 T_2}{4}},$$

and the approximation of low RF power $1 \gg \frac{\gamma^2 B_{\text{RF}}^2 T_1 T_2}{4}$, we arrive at the lineshapes for the transverse spin components

$$\begin{aligned}\tilde{S}_x(\omega_{\text{RF}}) &= S_0 B_{\text{RF}} \gamma \frac{\Gamma}{4[(\omega_{\text{RF}} - \Omega_L)^2 + \Gamma^2/4]}, \\ \tilde{S}_y(\omega_{\text{RF}}) &= S_0 B_{\text{RF}} \gamma \frac{(\Omega_L - \omega_{\text{RF}})}{2[(\omega_{\text{RF}} - \Omega_L)^2 + \Gamma^2/4]},\end{aligned}$$

which gives a Lorentzian (dispersive) lineshape centered on Ω_L for the \tilde{S}_x (\tilde{S}_y) component where the amplitude is linearly proportional to B_{RF} . Γ now represents the linewidth of the magnetometer response, otherwise known as the full-width at half-maximum (FWHM). In the lab frame, $S_x = \tilde{S}_x \cos(\omega_{\text{RF}} t) + \tilde{S}_y \sin(\omega_{\text{RF}} t)$, and therefore by probing in the x -axis, the imprinted polarisation rotation signal will be made up of the \tilde{S}_x component oscillating in-phase with the RF and the \tilde{S}_y component oscillating out-of-phase with the RF. Utilising a lock-in amplifier (LIA) or fast Fourier transform (FFT), it is possible to extract both lineshapes from the polarimetry signal.

9.2 Nuclear atomic resonance in our conditions

In this section, the response of an RF-AM is discussed. The solution to the Liouville equation for the evolution of the density matrix is required to fully describe the atomic system. This is introduced in Section 3.4.5. However, the response can be well described by the phenomenological Bloch equations [?]. This is derived below.

9.2.1 Bloch Equations Description

In this section, I modify the approach of Abragam (1961) [?] to analyze the behavior of an RF-AM.

Consider the total atomic spin vector, $\vec{F} = \{F_x, F_y, F_z\}$. \vec{F} is simply the sum of all the individual atomic spins that contribute to the magnetometer signal. The evolution of \vec{F} in an external magnetic field \vec{B} is given by:

$$\frac{d\vec{F}}{dt} = \gamma \vec{F} \times \vec{B} - \frac{F_x \hat{x} + F_y \hat{y}}{T_2} - \frac{F_z - F_0}{T_1} \hat{z}, \quad (13)$$

where $\hat{x}, \hat{y}, \hat{z}$ are the unit vectors in the laboratory frame and γ is the gyromagnetic ratio. The terms on the right-hand side of Equation 3.29 represent the equation of motion for free spins, the decay of any transverse spin components at a rate $1/T_2$ (where T_2 is the transverse relaxation time), and the trend towards an equilibrium value ($F_z = F_0$) in the z-direction at a rate $1/T_1$ (where T_1 is the longitudinal relaxation time).

For the RF-AM systems discussed here, T_2 is the transverse spin relaxation time, affected by processes such as alkali-alkali collisions, which are described in detail in Section 3.7. T_1 is effectively the optical pumping timescale, influenced by the frequency, power, and polarization of the pump beam.

The total field felt by the atoms is the sum of the static bias field and the RF field, $\vec{B} = \vec{B}_{\text{bias}} + \vec{B}_{\text{RF}}$. The bias field is applied along \hat{z} . This imposes a resonant Zeeman transition frequency, which I define as ω_0 , via the Zeeman effect:

$$\vec{B}_{\text{bias}} = B_{\text{bias}} \hat{z} = -\frac{\omega_0}{\gamma} \hat{z}. \quad (14)$$

The RF field is applied along the y -direction. Consider this field to be linearly polarized and oscillating at a frequency ω with an amplitude $2B_1 = \frac{2\omega_1}{\gamma}$ (i.e., $\vec{B}_{\text{RF}} = 2B_1 \cos \omega t$). Moving to the rotating frame about \hat{z} at frequency ω , the total effective field is:

$$\vec{B}_{\text{eff}} = \left(B_{\text{bias}} + \frac{\omega}{\gamma} \right) \hat{z} + B_1 \hat{y} = \frac{\Delta\omega \hat{z} + \omega_1 \hat{y}}{\gamma}, \quad (15)$$

where $\Delta\omega = (\omega - \omega_0)$ is the detuning of the RF field from resonance, and the unit vectors in the rotating frame are $\hat{x}', \hat{y}', \hat{z}' = \hat{z}$. The counter-rotating component of the RF field has been neglected in an implementation of the rotating wave approximation. In the rotating frame, the Bloch equations (Equation 3.29) become:

$$\frac{d\vec{F}'}{dt} = \gamma \vec{F}' \times \vec{B}_{\text{eff}} - \frac{F'_x \hat{x}' + F'_y \hat{y}'}{T_2} - \frac{F'_z - F_0}{T_1} \hat{z}', \quad (16)$$

where the tilde terms (\sim) denote the spin components in the rotating frame.

By combining Equations 3.31 and 3.32, the equations of motion for the spin components in the rotating frame are:

$$\begin{pmatrix} \frac{dF'_x}{dt} \\ \frac{dF'_y}{dt} \\ \frac{dF'_z}{dt} \end{pmatrix} = \begin{pmatrix} -\frac{1}{T_2} & \Delta\omega & -\omega_1 \\ -\Delta\omega & -\frac{1}{T_2} & 0 \\ \omega_1 & 0 & -\frac{1}{T_1} \end{pmatrix} \begin{pmatrix} F'_x \\ F'_y \\ F'_z \end{pmatrix} + \begin{pmatrix} 0 \\ 0 \\ \frac{F_0}{T_1} \end{pmatrix}. \quad (17)$$

The general solution is given by a series of exponential terms of the form $\vec{F}' = \vec{v} e^{\lambda t} + \vec{c}(t)$, where λ and \vec{v} are the eigenvalues and eigenvectors of the matrix.

9.2.2 Steady-State Solutions to the Bloch Equations

The operation of an RF-AM is a continuous process. Therefore, one can assume that sufficient time has elapsed to consider the steady-state solution of the Bloch equations. This is found by setting $\frac{dF'_x}{dt} = \frac{dF'_y}{dt} = \frac{dF'_z}{dt} = 0$ in Equation 3.33.

The resulting system of linear equations yields:

$$F'_x = \frac{\omega_1 T_2}{1 + \omega_1^2 T_1 T_2 + \Delta\omega^2 T_2^2} F_0, \quad (18)$$

$$F'_y = \frac{-\omega_1 \Delta\omega T_2^2}{1 + \omega_1^2 T_1 T_2 + \Delta\omega^2 T_2^2} F_0, \quad (19)$$

$$F'_z = \frac{1 + \Delta\omega^2 T_2^2}{1 + \omega_1^2 T_1 T_2 + \Delta\omega^2 T_2^2} F_0. \quad (20)$$

Finally, substituting $\omega_1 = \gamma B_1$ gives:

$$F'_x = \frac{\gamma B_1 T_2}{1 + \gamma^2 B_1^2 T_1 T_2 + \Delta\omega^2 T_2^2} F_0, \quad (21)$$

$$F'_y = \frac{-\gamma \Delta\omega B_1 T_2^2}{1 + \gamma^2 B_1^2 T_1 T_2 + \Delta\omega^2 T_2^2} F_0, \quad (22)$$

$$F'_z = \frac{1 + \Delta\omega^2 T_2^2}{1 + \gamma^2 B_1^2 T_1 T_2 + \Delta\omega^2 T_2^2} F_0. \quad (23)$$

9.2.3 Predicted Resonance Line Shapes

Returning to the laboratory frame, $F_x = F'_x \cos(\omega t) + F'_y \sin(\omega t)$. Note that it is this spin component that is detected by the probe beam. The RF-AM output thus comprises components oscillating in phase and in quadrature with respect to the driving field. These correspond to absorptive $\langle F'_x \rangle$ and

dispersive $\langle F'_y \rangle$ contributions. In practice, a dual-phase lock-in amplifier, referenced to the driving RF field at ω , is able to extract these two components from the probe beam.

The resonant line shapes refer to the shape of the components F'_x and F'_y as the driving RF field (ω) moves through the resonant frequency (ω_0). By defining:

$$\Gamma = \frac{2}{T_2} \sqrt{1 + \gamma^2 B_1^2 T_1 T_2}, \quad (24)$$

as the full-width-half-maximum (FWHM), it follows immediately that the line shapes are given by Lorentzian distributions of the form:

$$F'_x(\omega) = \frac{2A}{\pi} \frac{\Gamma}{4(\omega - \omega_0)^2 + \Gamma^2}, \quad (25)$$

$$F'_y(\omega) = \frac{2A}{\pi} \frac{\Gamma(\omega_0 - \omega)}{4(\omega - \omega_0)^2 + \Gamma^2}, \quad (26)$$

which are centered at the resonant frequency ω_0 . The absorptive $\langle F'_x \rangle$ component is a standard Lorentzian, whereas the dispersive $\langle F'_y \rangle$ component is an anti-Lorentzian function.

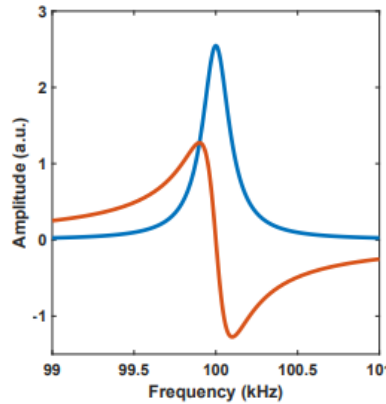


Figure 3.13: Example RF-AM resonance response: Theoretical plots of \tilde{F}_x (blue) and \tilde{F}_y (red). Centred at $\omega_0 = 100$ kHz with $\Gamma = 200$ Hz.

Figure 26: Example RF-AM resonance response: Theoretical plots of F'_x (blue) and F'_y (red). Centered at $\omega_0 = 100$ kHz with $\Gamma = 200$ Hz.

9.3 Helmholtz coil effect on the Zeeman Effect

In our case, the Zeeman effect is caused by the bias field in the Helmholtz coil :

$$\vec{B}(\vec{r}) = \frac{\mu_0}{4\pi} \int_C I d\vec{l} \times \frac{\hat{r} - \hat{r}'}{|\vec{r} - \vec{r}'|^3} \quad (\text{Biot-Savart Law for a general loop}) \quad (27)$$

$$B(z) = \frac{\mu_0 I}{4\pi} \int_{\text{spire}} \frac{R d\theta}{R^2 + z^2} \left(\frac{1}{(R^2 + z^2)^{3/2}} \right) \quad (\text{Field along the axis of a circular loop}) \quad (28)$$

$$\vec{B}_z = \frac{\mu_0 I R^2}{2(R^2 + z^2)^{3/2}} \hat{z} \quad (\text{Axial component due to symmetry}) \quad (29)$$

$$\vec{B} = \frac{\mu_0 I R^2}{2} \left(\frac{1}{[R^2 + (z+a)^2]^{3/2}} + \frac{1}{[R^2 + (z-a)^2]^{3/2}} \right) \hat{z} \quad (\text{Superposition of fields from shifted loops}) \quad (30)$$

$$\operatorname{div}(\vec{B}) = \frac{1}{r} \frac{\partial}{\partial r}(r B_r) + \frac{\partial B_z}{\partial z} \quad (\text{Divergence of } \mathbf{B}, \text{ showing that } \nabla \cdot \vec{B} = 0) \quad (31)$$

$$B_r = -\frac{r}{2} \frac{dB_{\text{axe}}}{dz} = \frac{3\mu_0 I R^2 z r}{4(R^2 + z^2)^{5/2}} \quad (\text{Radial component calculated via derivative}) \quad (32)$$